Whole-Body Diffusion Kurtosis Imaging: Initial Experience on Non-Gaussian Diffusion in Various Organs

Filli, Lukas ; Wurnig, Moritz ; Nanz, Daniel ; Luechinger, Roger ; Kenkel, David ; Boss, Andreas

DOI: https://doi.org/10.1097/RLI.0000000000000082

Whole-Body Diffusion Kurtosis Imaging

Initial Experience on Non-Gaussian Diffusion in Various Organs

Lukas Filli, MD, Moritz Wurnig, MD, MSc,* Daniel Nanz, PhD,* Roger Luechinger, PhD,† David Kenkel, MD,* and Andreas Boss, MD, PhD**

Introduction: Diffusion kurtosis imaging (DKI) is based on a non-Gaussian diffusion model that should inherently better account for restricted water diffusion within the complex microstructure of most tissues than the conventional diffusion-weighted imaging (DWI), which presumes Gaussian distributed water molecule displacement probability. The aim of this investigation was to test the technical feasibility of in vivo whole-body DKI, probe for organ-specific differences, and compare whole-body DKI and DWI results.

Materials and Methods: Eight healthy subjects underwent whole-body DWI on a clinical 3.0 T magnetic resonance imaging system. Echo-planar images in the axial orientation were acquired at b-values of 0, 150, 300, 500, and 800 mm^2/s. Parametrical whole-body maps of the diffusion coefficient (*D*), the kurtosis (*K*), and the traditional apparent diffusion coefficient (*ADC*) were generated. Goodness of fit was compared between DKI and DWI fits using the sums of squared residuals. Data groups were tested for significant differences of the mean by paired Student *t* tests.

Results: Good-quality parametrical whole-body maps of *D*, *K*, and *ADC* could be computed. Compared with *ADC* values, *D* values were significantly higher in the cerebral gray matter (by 30%) and white matter (27%), renal cortex (23%) and medulla (21%), spleen (101%), as well as erector spinae muscle (34%) (each *P* value <0.001). No significant differences between *D* and *ADC* were found in the cerebrospinal fluid ($P = 0.08$) and in the liver ($P = 0.13$). Curves of DKI fitted the measurement points significantly better than DWI curves did in most organs.

Conclusions: Whole-body DKI is technically feasible and may reflect tissue microstructure more meaningfully than whole-body DWI.

Key Words: whole body, diffusion kurtosis, DKI, diffusion-weighted imaging, magnetic resonance

(*Invest Radiol* 2014;49: 773–778)

Diffusion-weighted imaging (DWI) is a well-established clinical tool in magnetic resonance imaging (MRI). In the brain, its main applications include early detection of cerebral ischemia and characterization of focal brain lesions.[1] Within the last few years, the development of strong magnetic field gradient systems combined with parallel imaging techniques allowed the extension of DWI to applications in the body. Among these are the detection and characterization of malignant disease, such as lung cancer,[2] breast cancer,[3] primary and secondary liver malignancies,[4–6] renal cancer,[7] or prostate cancer.[8–11] The high cellular density in most tumors results in a water diffusion that is more restricted than in normal parenchyma or scar tissue.[12–14] The apparent diffusion coefficient (*ADC*), which is a quantitative measure of diffusion, is a biomarker that may be used in the assessment of aggressiveness of some malignant diseases, quantify early treatment response, and potentially even allow prediction of treatment response.

Modern MRI systems, which are equipped with a moving table platform and numerous receivers, are capable of whole-body imaging within a clinically acceptable measurement time. Whole-body DWI is an emerging tool for the detection and staging of widespread metastatic disease or lymphoma.[15–17] Whole-body DWI with background suppression is a young but promising alternative to positron emission tomography and computed tomography in different types of cancer.[18–22]

The determination of the ADC is based on the assumption of a Gaussian distribution of displacement probabilities of water molecules due to water self-diffusion. Unlike in isotropic liquid media, however, diffusion of water molecules in cellular tissue is restricted by barriers such as cellular membranes and intracellular organelles and, therefore, is not Gaussian in most tissues of the human body.[23,24] Imaging methods based on non-Gaussian diffusion models, such as diffusion kurtosis imaging (DKI), may assess the complexity of microstructural environments more accurately than conventional DWI.[25] The kurtosis quantifies the "non-Gaussianity" of the diffusion distribution and can be considered as a biomarker of the heterogeneity of tissue microstructure.[24]

Whereas early studies concentrated on non-Gaussian diffusion models in brain imaging,[26–31] recent publications also found additional value of DKI in the imaging of head and neck tumors,[32,33] non–small cell lung cancer,[34] hepatocellular carcinoma,[35] and prostate cancer.[36] In addition, DKI has been shown to reflect microstructural characteristics of renal tissue more accurately than conventional DWI.[37,38] These early but promising results raise the question whether in vivo DKI might also add valuable information to conventional DWI in whole-body imaging, for example, of widespread metastatic disease or systemic muscle disease. In the present study, initial results on the technical feasibility of an MRI protocol for whole-body DKI are presented and limitations of the current approach are discussed.

MATERIALS AND METHODS

Subjects

Eight healthy volunteers participated in this institutional review board–approved prospective study (4 men and 4 women; mean age, 30.6 years; range, 24–35 years). All individuals provided written informed consent before the magnetic resonance (MR) examination with agreement to the subsequent scientific evaluation of the data sets.

Imaging Protocol

Spin-echo prepared transverse echo-planar imaging data were acquired on a 3-T whole-body MR scanner (Ingenia; Philips Healthcare, Best, The Netherlands) with the integrated posterior coil, a 15-channel head coil, and a 32-channel flexible anterior coil during free breathing. Six stacks of axial slices with a field of view of 450 (*x* axis) × 295 (*y* axis) × 300 (*z* axis) mm^3 were acquired. Further sequence parameters were as follows: repetition time, 8708 milliseconds; echo time, 64 milliseconds; slice thickness, 6 mm; in-plane resolution,

Received for publication April 2, 2014; and accepted for publication, after revision, May 9, 2014.

From the *Department of Diagnostic and Interventional Radiology, University Hospital of Zurich, and †Institute for Biomedical Engineering, University and Swiss Federal Institute of Technology Zurich, Zurich, Switzerland.

The authors declare no conflicts of interest.

Reprints: Lukas Filli, MD, Department of Diagnostic and Interventional Radiology, University Hospital of Zurich, Ramistrasse 100, CH-8091 Zurich, Switzerland. E-mail: Lukas.Filli@usz.ch.

ISSN: 0020-9996/14/4912–0773

3.5 × 3.5 mm^2; echo-planar imaging factor, 29; sensitivity encoding (SENSE) factor, 3; and number of signal averages, 3. Fat signal was suppressed with an inversion pulse at an inversion time of 220 milliseconds. All images were acquired with 5 different b-values (0, 150, 300, 500, and 800 s/mm^2).

Postprocessing

The image stacks acquired in the axial orientation were composed of whole-body data sets for each b-value and reformatted coronally. Subsequently, parametrical maps of *ADC*, *D*, and *K* were calculated on a voxel-by-voxel basis by using in-house Matlab routines (The MathWorks, Natick, MA). The *ADC* was determined on the basis of the assumption of a monoexponential relationship between signal intensity S_b and b-value:

$$S(b) = S_0 \cdot \exp(-b \times ADC) \quad (1)$$

Diffusion kurtosis imaging quantifies the non-monoexponentiality of the diffusion by means of a second-order Taylor series expansion. To obtain voxelwise *D* and *K* values, the following equation was fitted to the signal decay curves:

$$S(b) = S_0 \cdot \exp(-bD + b^2D^2K/6) \quad (2)$$

A nonlinear Levenberg-Marquardt–based fit algorithm was used. To assess the goodness of fit for both DWI and DKI exponential analyses, the sum of the squared residuals was measured ("resnorm" of the Matlab routine "lsqcurvefit").

Measurements and Statistical Analysis

Parameters of DKI were measured by region-of-interest (ROI) analysis on axial images. In each case, 3 ROIs were placed in the cerebrospinal fluid (CSF, measured in the lateral ventricles), cerebral gray matter (GM, measured in the striatum) and white matter (WM, measured in the corona radiata), liver, renal cortex and medulla, spleen, as well as erector spinae muscle (at the level of the kidneys). Large vascular structures such as the hepatic veins were avoided in the definition of the ROIs.

Descriptive statistics and statistical comparisons were applied to the ROI analyses in Statistical Package for the Social Sciences (version 19; IBM Corp, Somers, NY). The Student *t* tests were used (1) to compare DKI and DWI parameters measured in different organs and (2) to compare the goodness of fit on the basis of the sum of the residuals of DKI and DWI curves. A *P* value of less than 0.05 was considered to indicate statistically significant differences.

RESULTS

Image Acquisition

All images were successfully acquired. Total whole-body scanning duration was approximately 45 minutes (7.5 minutes per stack).

Parametrical Maps

Examples of coronal and axial maps of DKI parameters and corresponding *ADC* values are shown in Figures 1 and 2. Different organs and compartments are readily recognized on these maps. Values of *D* were typically higher than ADC values in parenchymal soft tissue organs. Subcutaneous fatty tissue showed the highest *K* values; from among the parenchymal organs, the highest *K* values were observed in the spleen. *K* was close to zero in vessels and other low-viscuous fluid containing structures. The liver exhibited the highest *D* and *ADC* values (with large residuals indicating suboptimal fitting with both DWI and DKI analyses, presumably caused by perfusion effects). A small artificial corona could be observed, surrounding the skull in all parametrical maps, which was interpreted as a SENSE parallel imaging artifact.

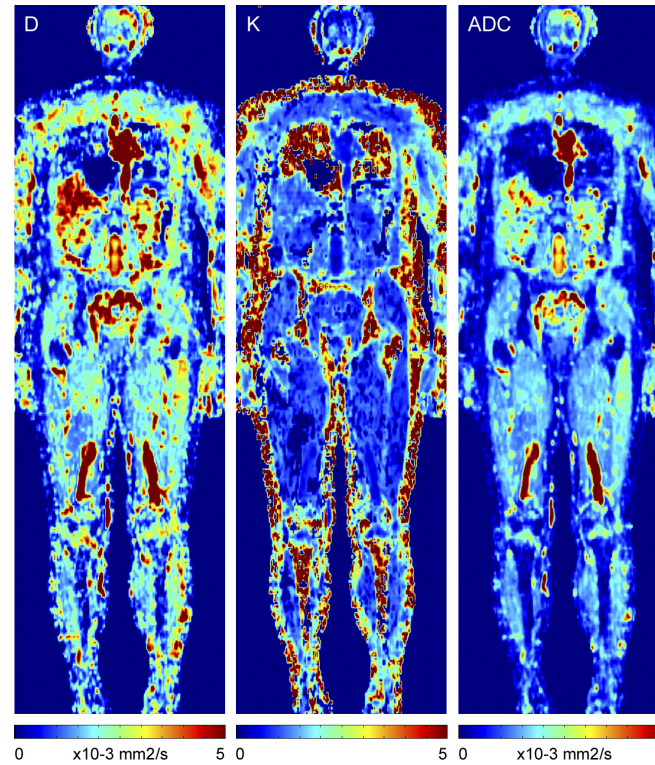

FIGURE 1. Sample whole-body maps of the *D* and *K* compared with *ADC* obtained from the monoexponential fitting.

Quantitative Measurements

Figure 3 illustrates typical signal intensity measurements in different organs and corresponding DKI and DWI fit curves. The DKI curves fitted the data points with smaller residuals (in the subsequent part of this section) compared with the monoexponential DWI approximation curves except for CSF, in which both curves were almost identical.

Mean values and standard deviation of the parameters measured in different organs are presented in Figure 4 and Table 1. *D* was significantly higher than *ADC* in the cerebral GM (30%) and WM (27%), renal cortex (23%) and medulla (21%), spleen (101%), as well as erector spinae muscle (34%) (*P* values each <0.001). No significant differences were found between *D* and *ADC* measured in the CSF ($P = 0.08$) and in the liver ($P = 0.13$).

In the brain, the mean value of *K* was higher in WM than in GM; however, the difference was not statistically significant ($P = 0.2$). Measurements in the liver revealed significantly higher *D* and lower *K* values than in the other organs ($P < 0.001$ each) and also compared with the CSF (*D*, $P = 0.008$; *K*, $P < 0.001$). Between the renal cortex and medulla, no significant difference was found in *D* ($P = 0.2$), *K* ($P = 0.9$), and *ADC* ($P = 0.054$).

The mean resnorm values of the DWI curves generated in all volunteers were between 1.5-fold (GM) and 3.6-fold (muscle) higher than those of the DKI curves, indicating a better fit of the DKI curves to the measurement points. This difference was statistically significant in WM, liver, renal cortex, and medulla as well as muscle (for *P* values, see Table 1).

DISCUSSION

The present study reports on initial experiences with the feasibility of whole-body DKI in humans using a clinical MR scanner. Whole-body data sets could be obtained within an acceptable measurement

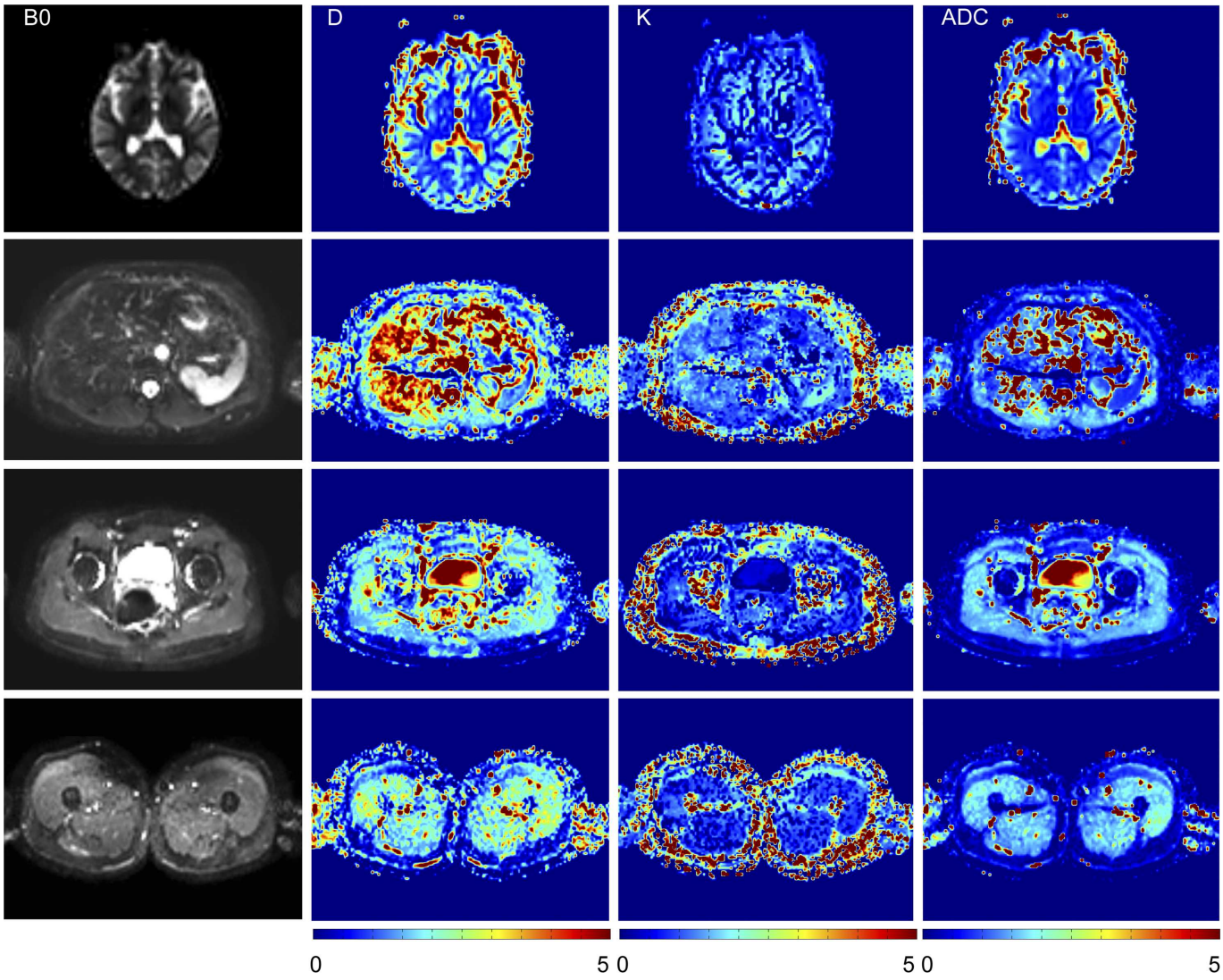

FIGURE 2. Axial B_0 diffusion images and parametrical maps of the DK *D*, the DK *K* representing the non-Gaussian water molecular diffusion, and the conventional *ADC* of DWI at 4 different table positions are provided.

time. The DKI algorithm described in previous studies[24] was applied on a voxel-by-voxel basis to obtain parametrical whole-body maps of the *D* and *K*. The results of this study suggest that DKI is applicable to whole-body imaging and that DKI, in general, provides a better description of the diffusion data sets compared with DWI.

By quantifying the non-Gaussianity of the diffusion distribution in DWI, *K* is a comparatively direct measure of the heterogeneity of tissue microstructure.[24] Recent studies, which focused on single organs, reported that DKI may reflect microstructural conditions more accurately compared with conventional DWI.[23,25,36,37] These promising results kindle an interest in whole-body DKI in vivo because

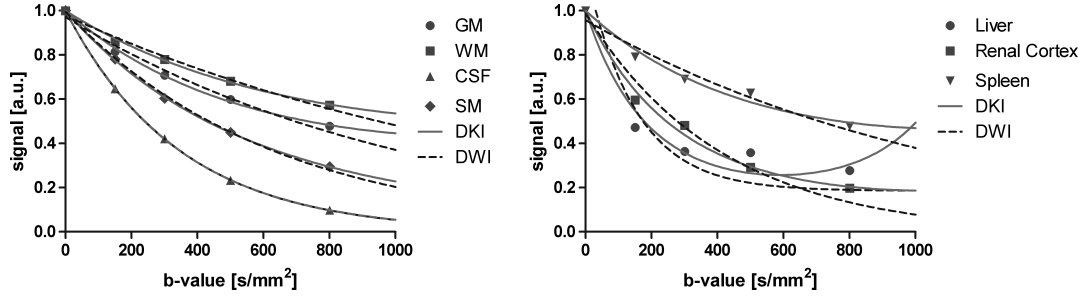

FIGURE 3. Typical curves of signal intensity as a function of the b-value, measured in the ROIs in different organs of 1 subject, and the corresponding DKI and DWI fit curves. In liver tissue, an increasing DKI curve at b greater than 800 s/mm^2 can be noticed.

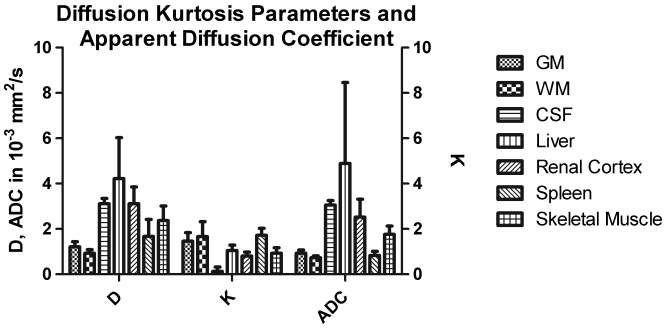

FIGURE 4. Bar diagram of DKI parameters (*D*, *K*) and the *ADC* for various organs.

this technique may allow more comprehensive tissue characterization compared with conventional whole-body DWI in the assessment of systemic oncological or inflammatory diseases.

Technical Aspects

Precision and accuracy of calculated DKI parameters (*D*, *K*) depend on the number and levels of b-values applied. In terms of levels, a maximum b-value of 2000 to 2500 s/mm^2 is typically suggested in DKI studies of the brain.[25] In other regions of the body, however, the use of such high b-values is limited by a low signal-to-noise ratio (SNR) because of the lower sensitivity of flexible surface coils compared with the head coil. Another important factor is the lower T2 transverse relaxation time in most other tissues compared with the brain resulting in a faster decay of the transverse relaxation. This faster signal decay precludes the application of such high b-values in the body trunk because of 2 effects: (1) the long echo time of the echo-planar imaging sequence due to the longer application of the diffusion gradients and (2) the strong signal attenuation in DWI using high b-values. Furthermore, many tissues exhibit higher ADC values compared with the brain, again resulting in faster signal decay.

In previous studies on DKI of the kidney, a maximum b-value of 600 to 800 s/mm^2 was found to be sufficient for DKI parameter estimation.[37,38] On the basis of these studies, we chose a maximum b-value of 800 s/mm^2 as a compromise between appropriate SNR and quantification accuracy of DKI parameters. To ensure sufficient SNR, a relatively high SENSE parallel imaging factor providing a short echo time (64 milliseconds) was chosen; furthermore, the acquisition of 3 signal averages was applied. To reduce potential noise effects and thus ensure good approximation of the curve fit, we applied 5 instead of the theoretical minimum of 3 different b-values, with the disadvantage of longer scanning duration.

We found that, compared with DWI curves, DKI curves fitted the measurement points with significantly smaller residuals in most parenchymal organs, which can be explained by the higher number of fit variables. These findings are in accordance with previous reports on single organs.[36] The residuals in abdominal organs were, in general, higher than those in the brain for both DKI and DWI analyses, which may, in part, be attributed to breathing motion and, in the special case of the liver, are a significant contribution of microcirculation (intravoxel incoherent motion) to the signal curves. Further evidence for the validity of the DKI model may be obtained by comparing the relative confidence intervals of the fitted parameters; although such a detailed error analysis might be instructive in the future, it shall not extend the size of the present study.

A major challenge of whole-body DKI lies in the long scanning duration. By acquiring only the minimum of 3 b-values, the scanning duration could be shortened to 27 minutes. Moreover, by not evaluating the lower extremities, another 50% of time could potentially be saved.

Results and Comparison With the Literature

The parametrical whole-body maps generated in the present study readily allow depiction of different anatomic landmarks and compartments. In accordance with earlier observations,[27,32] *D*, which is corrected for non-Gaussian diffusion distribution, was higher than the conventional, monoexponentially determined *ADC* in most tissues. Larger *K* values were found in subcutaneous tissue, which seems reasonable because the microarchitecture of this tissue is dominated by lipid storage with a strongly restricted space for water diffusion. In the brain, despite the relatively low maximum b-value of 800 s/mm^2, the *K* of the WM tended to be higher than that in the GM. This difference was not statistically significant, which is probably because of partial volume effects caused by the lower spatial resolution compared with dedicated brain examinations. However, the order of the observed parametrical values is consistent with previous observations.[25]

In the liver, abnormally high *D* and *ADC* values were measured compared with previous observations. Because respiratory triggering was not possible given the long scan duration, these parameters may have been influenced by free breathing. Despite the short echo time, the motion of dephasing spins during the image acquisition may have led to an overestimation of *D* and *ADC*. However, we believe that this effect was much smaller compared with the influence of perfusion effects from intravoxel incoherent motion, mainly of microcirculation from portal venous flow, which is a unique feature of the liver. The

TABLE 1. Mean (SD) Values for DKI and DWI Parameters for Different Tissues and Corresponding Mean Sums of Squared Residuals

	DKI			DWI		resnorm
Tissue	*D* [10^{-3} mm^2/s]	*K*	resnorm [$\times 10^{-3}$]	*ADC* [10^{-3} mm^2/s]	resnorm [$\times 10^{-3}$]	Difference (*P*)
GM	1.21 (0.22)	1.46 (0.38)	0.15 (0.18)	0.93 (0.15)	0.23 (0.19)	0.099
WM	0.93 (0.16)	1.66 (0.67)	0.13 (0.20)	0.73 (0.09)	0.63 (0.57)	0.013
CSF	3.11 (0.23)	0.13 (0.19)	0.16 (0.26)	3.06 (0.19)	0.53 (0.62)	0.150
Liver	4.22 (1.80)	1.04 (0.25)	10.69 (7.78)	4.88 (3.58)	38.51 (28.37)	0.009
Renal cortex	3.11 (0.75)	0.80 (0.18)	2.83 (2.29)	2.52 (0.79)	12.49 (12.76)	0.048
Renal medulla	2.98 (1.03)	0.79 (0.21)	1.87 (1.46)	2.47 (0.98)	8.05 (5.41)	0.009
Spleen	1.67 (0.75)	1.72 (0.32)	10.58 (7.67)	0.83 (0.18)	22.90 (25.37)	0.171
Muscle	2.37 (0.65)	0.93 (0.25)	1.69 (1.27)	1.77 (0.36)	7.78 (6.12)	0.010

The right column shows the statistical difference between the resnorms of DKI and DWI curves.

ADC indicates apparent diffusion coefficient; CSF, cerebrospinal fluid; DKI, diffusion kurtosis imaging; DWI, diffusion-weighted imaging; GM, gray matter; resnorm, measure of goodness of fit; WM, white matter.

reason for this assumption is that such high *D* and *ADC* values were not observed in other parenchymal abdominal organs that also exhibit notable breathing motion, such as the kidneys.

The fitted DKI curve for the liver showed a nonphysical behavior of increasing signal at larger b-values. This is based on the 2 different signs (− and +) of the 2 terms in the argument of the exponential function in equation[2]: if the second term becomes dominant, for example, because of noise variability in the signal values or because of perfusion contributions, nonphysical behavior may occur. Therefore, it is crucial for the DKI model to include high b-values to minimize the influence of intravoxel incoherent motion and to "bind" the vertex of the exponential curve to high b-values. On the basis of former studies, we used a maximum b-value of 800 s/mm^2, which turned out to be a good compromise for different organs but apparently insufficient for liver imaging. Therefore, quantitative values of the liver have to be interpreted carefully.

The *ADC* values measured in the kidneys lay well within the range of 1.5 to 3.0 × 10^{-3} mm^2/s reported for normal renal parenchyma.[39] Furthermore, it is known that *ADC* values do not differ significantly between the cortex and medulla when relatively low b-values are used, likely because of the compensation of greater anisotropy in the medulla by higher true diffusion.[40] In distinction to recent studies,[37,38] however, corticomedullary differentiation based on DKI parameter values was not possible in the present study. A possible explanation may again be the superposition of effects from respiratory motion.

The kurtosis of the spleen was significantly higher than that of other abdominal organs, indicating high microstructural heterogeneity in the spleen of healthy subjects. Changes of *ADC* in the spleen have been observed in patients with liver cirrhosis and portal hypertension.[41,42] Future studies may provide more comprehensive characterization of the spleen by taking into account the non-Gaussian diffusion in the spleen.

Measurement of the structural anisotropy of skeletal muscle is of growing interest[43,44] and has been shown to allow differentiation between neurogenic and myopathic disease.[45] In the erector spinae muscle, we measured an intermediate kurtosis of 0.93 ± 0.25 and a strong decrease in the residuals of the fit using the DKI analysis compared with conventional DWI analysis, indicating a significant contribution of non-Gaussian diffusion in muscle tissue. This finding might constitute a starting point for future investigations on the value of DKI for the assessment of muscle diseases.

CONCLUSIONS

In conclusion, our initial experiences show that whole-body DKI is technically feasible within an acceptable measurement time. The DKI model fitted the data with significantly smaller residuals. Whole-body DKI measurements may be of future interest in research on widespread disease for in-depth characterization of diffusion properties of tissues.

REFERENCES

1. Mascalchi M, Filippi M, Floris R, et al. Diffusion-weighted MR of the brain: methodology and clinical application. *Radiol Med*. 2005;109:155–197.
2. Nomori H, Mori T, Ikeda K, et al. Diffusion-weighted magnetic resonance imaging can be used in place of positron emission tomography for N staging of non-small cell lung cancer with fewer false-positive results. *J Thorac Cardiovasc Surg*. 2008;135:816–822.
3. Woodhams R, Matsunaga K, Iwabuchi K, et al. Diffusion-weighted imaging of malignant breast tumors: the usefulness of apparent diffusion coefficient (ADC) value and ADC map for the detection of malignant breast tumors and evaluation of cancer extension. *J Comput Assist Tomogr*. 2005;29:644–649.
4. Wagner M, Doblas S, Daire JL, et al. Diffusion-weighted MR imaging for the regional characterization of liver tumors. *Radiology*. 2012;264:464–472.
5. d'Assignies G, Fina P, Bruno O, et al. High sensitivity of diffusion-weighted MR imaging for the detection of liver metastases from neuroendocrine tumors: comparison with T2-weighted and dynamic gadolinium-enhanced MR imaging. *Radiology*. 2013;268:390–399.
6. Doblas S, Wagner M, Leitao HS, et al. Determination of malignancy and characterization of hepatic tumor type with diffusion-weighted magnetic resonance imaging: comparison of apparent diffusion coefficient and intravoxel incoherent motion-derived measurements. *Invest Radiol*. 2013;48:722–728.
7. Chandarana H, Kang SK, Wong S, et al. Diffusion-weighted intravoxel incoherent motion imaging of renal tumors with histopathologic correlation. *Invest Radiol*. 2012;47:688–696.
8. Kobus T, Vos PC, Hambrock T, et al. Prostate cancer aggressiveness: in vivo assessment of MR spectroscopy and diffusion-weighted imaging at 3 T. *Radiology*. 2012;265:457–467.
9. Concia M, Sprinkart AM, Penner AH, et al. Diffusion-weighted magnetic resonance imaging of the pancreas: diagnostic benefit from an intravoxel incoherent motion model-based 3 b-value analysis. *Invest Radiol*. 2014;49:93–100.
10. Somford DM, Hoeks CM, Hulsbergen-van de Kaa CA, et al. Evaluation of diffusion-weighted MR imaging at inclusion in an active surveillance protocol for low-risk prostate cancer. *Invest Radiol*. 2013;48:152–157.
11. Maas MC, Futterer JJ, Scheenen TW. Quantitative evaluation of computed high B value diffusion-weighted magnetic resonance imaging of the prostate. *Invest Radiol*. 2013;48:779–786.
12. Kim CK, Park BK, Han JJ, et al. Diffusion-weighted imaging of the prostate at 3 T for differentiation of malignant and benign tissue in transition and peripheral zones: preliminary results. *J Comput Assist Tomogr*. 2007;31:449–454.
13. Kim JK, Kim KA, Park BW, et al. Feasibility of diffusion-weighted imaging in the differentiation of metastatic from nonmetastatic lymph nodes: early experience. *J Magn Reson Imaging*. 2008;28:714–719.
14. Perrone A, Guerrisi P, Izzo L, et al. Diffusion-weighted MRI in cervical lymph nodes: differentiation between benign and malignant lesions. *Eur J Radiol*. 2011;77:281–286.
15. Li S, Xue HD, Li J, et al. Application of whole body diffusion weighted MR imaging for diagnosis and staging of malignant lymphoma. *Chin Med Sci J*. 2008;23:138–144.
16. Eiber M, Holzapfel K, Ganter C, et al. Whole-body MRI including diffusion-weighted imaging (DWI) for patients with recurring prostate cancer: technical feasibility and assessment of lesion conspicuity in DWI. *J Magn Reson Imaging*. 2011;33:1160–1170.
17. Kalkmann J, Lauenstein T, Stattaus J. Whole-body diffusion-weighted imaging in oncology: technical aspects and practical relevance [in German]. *Radiologe*. 2011;51:215–219.
18. Kwee TC, Takahara T, Ochiai R, et al. Diffusion-weighted whole-body imaging with background body signal suppression (DWIBS): features and potential applications in oncology. *Eur Radiol*. 2008;18:1937–1952.
19. Takahara T, Imai Y, Yamashita T, et al. Diffusion weighted whole body imaging with background body signal suppression (DWIBS): technical improvement using free breathing, STIR and high resolution 3D display. *Radiat Med*. 2004;22:275–282.
20. Stephane V, Samuel B, Vincent D, et al. Comparison of PET-CT and magnetic resonance diffusion weighted imaging with body suppression (DWIBS) for initial staging of malignant lymphomas. *Eur J Radiol*. 2013;82:2011–2017.
21. Kachewar SG. Using DWIBS MRI technique as an alternative to bone scan or PET scan for whole-body imaging in oncology patients. *Acta Radiol*. 2011;52:788.
22. Cafagna D, Rubini G, Iuele F, et al. Whole-body MR-DWIBS vs. [18F]-FDG-PET/CT in the study of malignant tumors: a retrospective study. *Radiol Med*. 2012;117:293–311.
23. Grinberg F, Farrher E, Ciobanu L, et al. Non-gaussian diffusion imaging for enhanced contrast of brain tissue affected by ischemic stroke. *PLoS One*. 2014;9:e89225.
24. Jensen JH, Helpern JA, Ramani A, et al. Diffusional kurtosis imaging: the quantification of non-gaussian water diffusion by means of magnetic resonance imaging. *Magn Reson Med*. 2005;53:1432–1440.
25. Jensen JH, Helpern JA. MRI quantification of non-Gaussian water diffusion by kurtosis analysis. *NMR Biomed*. 2010;23:698–710.
26. Alexander DC, Barker GJ, Arridge SR. Detection and modeling of non-Gaussian apparent diffusion coefficient profiles in human brain data. *Magn Reson Med*. 2002;48:331–340.
27. Lu H, Jensen JH, Ramani A, et al. Three-dimensional characterization of non-gaussian water diffusion in humans using diffusion kurtosis imaging. *NMR Biomed*. 2006;19:236–247.
28. Falangola MF, Jensen JH, Babb JS, et al. Age-related non-Gaussian diffusion patterns in the prefrontal brain. *J Magn Reson Imaging*. 2008;28:1345–1350.
29. Hui ES, Cheung MM, Qi L, et al. Advanced MR diffusion characterization of neural tissue using directional diffusion kurtosis analysis. *Conf Proc IEEE Eng Med Biol Soc*. 2008;2008:3941–3944.
30. Hui ES, Cheung MM, Qi L, et al. Towards better MR characterization of neural tissues using directional diffusion kurtosis analysis. *Neuroimage*. 2008;42:122–134.
31. Cheung MM, Hui ES, Chan KC, et al. Does diffusion kurtosis imaging lead to better neural tissue characterization? A rodent brain maturation study. *Neuroimage*. 2009;45:386–392.

32. Jansen JF, Stambuk HE, Koutcher JA, et al. Non-gaussian analysis of diffusion-weighted MR imaging in head and neck squamous cell carcinoma: a feasibility study. *AJNR Am J Neuroradiol*. 2010;31:741–748.
33. Yuan J, Yeung DK, Mok GS, et al. Non-Gaussian analysis of diffusion weighted imaging in head and neck at 3T: a pilot study in patients with nasopharyngeal carcinoma. *PLoS One*. 2014;9:e87024.
34. Heusch P, Kohler J, Wittsack HJ, et al. Hybrid [(1)(8)F]-FDG PET/MRI including non-Gaussian diffusion-weighted imaging (DWI): preliminary results in non-small cell lung cancer (NSCLC). *Eur J Radiol*. 2013;82: 2055–2060.
35. Rosenkrantz AB, Sigmund EE, Winnick A, et al. Assessment of hepatocellular carcinoma using apparent diffusion coefficient and diffusion kurtosis indices: preliminary experience in fresh liver explants. *Magn Reson Imaging*. 2012;30: 1534–1540.
36. Rosenkrantz AB, Sigmund EE, Johnson G, et al. Prostate cancer: feasibility and preliminary experience of a diffusional kurtosis model for detection and assessment of aggressiveness of peripheral zone cancer. *Radiology.* 2012;264: 126–135.
37. Pentang G, Lanzman RS, Heusch P, et al. Diffusion kurtosis imaging of the human kidney: a feasibility study. *Magn Reson Imaging*. 2014;32:413–420.
38. Wittsack HJ, Lanzman RS, Mathys C, et al. Statistical evaluation of diffusion-weighted imaging of the human kidney. *Magn Reson Med*. 2010; 64:616–622.
39. Gurses B, Kilickesmez O, Tasdelen N, et al. Diffusion tensor imaging of the kidney at 3 Tesla MRI: normative values and repeatability of measurements in healthy volunteers. *Diagn Interv Radiol*. 2011;17:317–322.
40. Thoeny HC, De Keyzer F, Oyen RH, et al. Diffusion-weighted MR imaging of kidneys in healthy volunteers and patients with parenchymal diseases: initial experience. *Radiology.* 2005;235:911–917.
41. Do RK, Chandarana H, Felker E, et al. Diagnosis of liver fibrosis and cirrhosis with diffusion-weighted imaging: value of normalized apparent diffusion coefficient using the spleen as reference organ. *AJR Am J Roentgenol*. 2010; 195:671–676.
42. Klasen J, Lanzman RS, Wittsack HJ, et al. Diffusion-weighted imaging (DWI) of the spleen in patients with liver cirrhosis and portal hypertension. *Magn Reson Imaging*. 2013;31:1092–1096.
43. Scheel M, Prokscha T, von Roth P, et al. Diffusion tensor imaging of skeletal muscle—correlation of fractional anisotropy to muscle power. *Rofo*. 2013;185: 857–861.
44. Schwenzer NF, Steidle G, Martirosian P, et al. Diffusion tensor imaging of the human calf muscle: distinct changes in fractional anisotropy and mean diffusion due to passive muscle shortening and stretching. *NMR Biomed*. 2009; 22:1047–1053.
45. Garmirian LP, Chin AB, Rutkove SB. Discriminating neurogenic from myopathic disease via measurement of muscle anisotropy. *Muscle Nerve*. 2009; 39:16–24.

